

# THE EFFECT OF A SOLID BOUNDARY ON THE PROPAGATION OF THERMODYNAMIC DISTURBANCES IN A RAREFIED GAS

Y. Ben-Ami and A. Manela<sup>1</sup>

Faculty of Aerospace Engineering, Technion - Israel Institute of Technology  
Haifa 32000 , Israel

July 6, 2020; revised August 11, 2020

---

Running title: Effect of a boundary on the propagation of thermodynamic disturbances in a rarefied gas  
40 pages and 7 figures  
Available in L<sup>A</sup>T<sub>E</sub>X 2<sub>ε</sub>

---

<sup>1</sup>email address for correspondence: amanela@technion.ac.il

## Abstract

We study the effect of a rigid boundary on the propagation of thermodynamic disturbances in a gas at non-continuum conditions. We consider a semi-infinite setup confined by an infinite planar wall and introduce initial gas disturbances in the form of density and temperature inhomogeneities. The problem is formulated for arbitrary small-amplitude perturbations, and analyzed in the entire range of gas rarefaction rates, governed by the Knudsen (Kn) number. Our results describe the system relaxation to equilibrium, with specific emphasis on the effect of the solid surface. Analytical solutions are obtained in the free-molecular and near-continuum (based on the Navier-Stokes-Fourier and regularized thirteen moment equations) regimes and compared with direct simulation Monte Carlo results. The impact of the solid wall is highlighted by comparing between diffuse (adiabatic or isothermal) and specular boundary reflections. Focusing on a case of an initial temperature disturbance, the results indicate that the system relaxation time shortens with increasing Kn. The isothermal boundary consistently reverberates the weakest acoustic disturbance, as the energy carried by the impinging wave is partially absorbed by the surface. The specular and adiabatic wall systems exhibit identical responses in the continuum limit, while departing with increasing Kn due to higher-order moment effects. The unsteady normal force exerted by the gas on the surface is quantified and analyzed.

# 1 Introduction

The characterization of acoustic reflection and absorption at a solid surface is a canonical problem in continuum-flow acoustics which has been studied extensively over the years [1]. The fundamental problem of interest is the interaction of incident small-amplitude disturbances, or a local point source, with a rigid boundary. Traditional works have considered the effects of the surface geometrical and impedance properties on its acoustic transmission. Recent progress has been motivated by the primary need for designing “acoustically invisible” structures, for which, at given flow conditions, the surface location cannot be identified through its acoustic scattering [2].

In cases where sound propagation in gases is considered at length- or time-scale that are of the order of the molecular mean free path or time, respectively, the continuum description breaks down and the system should be treated in the framework of gas kinetic theory. Prompted by small-scale and low-pressure evolving technologies, acoustic wave propagation in rarefied gases has been studied in a considerable number of works, beginning in the middle of the twentieth century and continuing to current and ongoing research (e.g., Refs. [3–16]). Primarily, these works have focused on a setup of a planar wall undergoing small-amplitude mechanical [4–7, 10, 11, 13–15] or thermal [9, 12, 14, 16] excitations, where the actuated surface was identified as the system source of sound. Other studies have considered the propagation of acoustic waves in narrow (micro-/nano-scale) channels [8, 17–20]). Driven by time-harmonic particle influx, the sources modeled in these investigations effectively mimic vibroacoustic sound generation, similarly to the above-mentioned oscillating wall systems.

Motivated by a different topic of interest, several researchers have analyzed the propagation of *flow-induced* disturbances in rarefied gases. Specifically, setups with gas-fluidic thermal sources, having a fundamental relevance in the fields of microscale heat transfer [21, 22] and ultrafast heating processes [23], have been considered. Logan [24], and later on Berkovsky and Bashtovoi [25], focused on the propagation of thermal disturbances in a non-confined gas, based on Grad’s moment equations and other model approximations of the Boltzmann equation. Follow-up investigations have addressed the expansion of heat sources in the vicinity of boundaries, yet were limited to the continuum limit of exceedingly small Knudsen numbers [26, 27]. The gas

response to local compression has been studied by Danforth and Long [28], who allowed large initial perturbations, but assumed a non-confined setup and focused on numerical simulations at near-continuum states.

Acknowledging the above, the objective of the present work is to investigate the effect of a rigid boundary on the propagation of gas-induced acoustic disturbances at non-continuum conditions. To this end, we consider a semi-infinite gas expanse confined by an infinite planar wall and introduce initial thermodynamic disturbances in the fluid. The small-amplitude disturbances are prescribed as either initial density or temperature inhomogeneities, which may physically occur due to gas local compression or heating, respectively. The problem is formulated for arbitrary small-amplitude initial perturbations, and analyzed in the entire range of gas rarefaction levels. Following the gas evolution in time and space, our results describe the system relaxation to equilibrium, with specific emphasis on the effect of the solid surface. Analytical solutions are obtained in the free-molecular and near-continuum (based on the Navier-Stokes-Fourier and regularized moment equations) regimes and compared with direct simulation Monte Carlo predictions. The impact of the solid wall is highlighted by comparing between the non-confined and confined gas responses with different surface conditions, including fully diffuse (adiabatic or isothermal) and fully specular wall reflections. Ideally, obtaining an “acoustically invisible” surface should be equivalent to recapturing the reference unbounded gas response in the presence of a cloaked wall. While this is not addressed here, the present analysis may be considered as a first step in this direction, through preliminary analysis of the impact of different wall conditions on the boundary acoustic reverberation.

In the next section, the problem is stated. The free-molecular limit is considered in Sec. 3, and the near-continuum regime is analyzed in Sec. 4. Description of the direct simulation Monte Carlo scheme, used to validate our findings, is given in Sec. 5. Our results are discussed in Sec. 6, followed by concluding comments in Sec. 7. Technical details regarding the free-molecular solution are relegated to Appendices.

## 2 Statement of the Problem

Consider a semi-infinite expanse of a monatomic gas, set at  $x^* > 0$  and confined by an infinite solid boundary at  $x^* = 0$  (hereafter, asterisks denote dimensional quantities). At time  $t^* = 0$ , the gas is maintained at rest, with given distributions of its local density and temperature fields,

$$\rho^*(x^*, 0) = \rho_0^* + \varepsilon \rho_{\text{in}}^*(x^*) \quad \text{and} \quad T^*(x^*, 0) = T_0^* + \varepsilon T_{\text{in}}^*(x^*), \quad (1)$$

respectively. In Eq. (1), it is assumed that  $\varepsilon \ll 1$ , where the gas is only slightly perturbed about its equilibrium state of uniform density  $\rho_0^*$  and temperature  $T_0^*$ , and the system linearized response is considered. Such scenarios may occur due to any small thermodynamic non-uniformities imposed by external disturbances of local compression or heating.

The work analyzes the effect of the solid boundary on the propagation of gas initial disturbances, specified above, following through the system final equilibrium state. To this end, we compare between perfectly reflecting (specular) and fully diffuse (adiabatic or isothermal) wall surfaces. These two extreme cases may be considered as limit realizations of completely reflecting and accommodating boundaries, respectively. Diffuse scattering takes place over “rough” surfaces, where the colliding particles attain thermal equilibrium with the reflecting wall and evaporate accordingly. Specular interactions occur when the incident molecules collide with a solid surface and rebound elastically as if hitting a perfectly smooth wall. While none of these idealized scenarios exists in reality, it is commonly accepted that wall reflections from “engineering” surfaces may be described, in a variety of applications, as a combination of diffuse and specular interactions, as formulated in the commonly-applied Maxwell-type condition [29]. In the present context, the combined diffuse-specular case merely superposes the above two limits, and is therefore not discussed in detail.

Considering the problem formulation in the adiabatic and isothermal surface configurations, the wall heat-flux  $q_{\text{wall}}^*$  and temperature  $T_{\text{wall}}^*$  are prescribed by

$$q_{\text{wall}}^* = 0 \quad \text{or} \quad T_{\text{wall}}^* = T_0^*, \quad (2)$$

respectively. To realize the isothermal boundary condition, it is assumed that the boundary is attached to a heat reservoir at a constant temperature. Conversely, an adiabatic condition may

be enforced using a heat-insulating wall having vanishing heat conductivity. In the other extreme of a perfectly reflecting wall, the gas response may be conveniently formulated by superposing the counterpart gas evolution in an unbounded domain (to be derived hereafter) with its symmetrical image about the surface location. In both diffuse and specular setups, a dimensionless description of the problem is obtained by scaling the position by a length-scale  $L^*$  characterizing the prescribed initial disturbance, the velocity by the mean thermal speed of a gas molecule  $U_{\text{th}}^* = \sqrt{2\mathcal{R}^*T_0^*}$  (with  $\mathcal{R}^*$  denoting the specific gas constant), and the time by the consequent time-scale  $L^*/U_{\text{th}}^*$ . The density and temperature are scaled by  $\rho_0^*$  and  $T_0^*$ , respectively, the pressure by  $\rho_0^*\mathcal{R}^*T_0^*$  and the heat flux by  $\rho_0^*U_{\text{th}}^{*3}$ . The non-dimensional problem is governed by the scaled initial disturbances  $\rho_{\text{in}}(x)$  and  $T_{\text{in}}(x)$ , together with the Knudsen number

$$\text{Kn} = l^*/L^*, \quad (3)$$

marking the ratio between the mean free path of a gas molecule and the system characteristic length-scale. An explicit expression for the gas molecular mean free path  $l^*$ , and subsequently to Kn, is given after Eq. (21), where the kinetic law of molecular interaction is specified.

The above-described diffuse- and specular-wall systems are analyzed in Secs. 3 and 4, where the limit cases of collision-free and near-continuum regimes are investigated. The reference case of gas relaxation in an unbounded domain is used to identify the impact of the solid surface. Analytical limit-case solutions are compared with direct simulation Monte Carlo (DSMC) predictions, to test their validity, and cover the entire range of gas rarefaction rates. As demonstrated in Sec. 6, the prevailing gas regime is governed by both the value of the Knudsen number and the time elapsed since the initial disturbance has been applied. Specifically, at times much shorter or longer than the mean free time,  $t_{\text{coll}}^* \approx l^*/U_{\text{th}}^*$ , the expected flow regime should turn free-molecular ( $t/\text{Kn} \ll 1$ ) or near-continuum ( $t/\text{Kn} \gg 1$ ), respectively. Transition between the two limits is expected at intermediate  $t/\text{Kn} \sim O(1)$  times.

### 3 Free-molecular limit

In the framework of gas kinetic theory and the unsteady one-dimensional configuration considered, the gas state is governed by the probability density function  $f = f(x, t, \xi)$  of finding a gas molecule with velocity about  $\xi = (\xi_x, \xi_y, \xi_z)$  at a position near  $x$  at time  $t$ . At the linearized conditions assumed we write

$$f(x, t, \xi) = F[1 + \varepsilon \phi(x, t, \xi)], \quad (4)$$

where  $F = \pi^{-3/2} \exp[-\xi^2]$  denotes the non-dimensional Maxwellian equilibrium distribution, and  $\phi(x, t, \xi)$  marks the probability perturbation function [30]. Assuming the Knudsen number to be large, we consider the collisionless one-dimensional unsteady Boltzmann equation for  $\phi(x, t, \xi)$ ,

$$\frac{\partial \phi}{\partial t} + \xi_x \frac{\partial \phi}{\partial x} = 0 \quad (5)$$

The equation is supplemented by the initial condition

$$\phi(x, 0, \xi) = \phi_{\text{in}}(x, \xi), \quad (6)$$

which, in accordance with Eq. (1), takes the linearized form of deviation from the equilibrium distribution

$$\phi_{\text{in}}(x, \xi) = \rho_{\text{in}}(x) + T_{\text{in}}(x)(\xi^2 - 3/2). \quad (7)$$

The probability perturbation function is additionally subject to a far-field decay condition and a boundary condition imposed at the solid wall. For the case of a fully diffuse (adiabatic or isothermal) boundary, the latter takes the linearized half-range form

$$\phi(0, t, \xi \cdot \hat{\mathbf{x}} > 0) = \rho_w(t) + T_w(t)(\xi^2 - 3/2), \quad (8)$$

where  $\hat{\mathbf{x}}$  is a unit vector directed in the positive  $x$ -direction (normal to the wall) and  $T_w(t)$  marks the time perturbation of the wall temperature. For an isothermal wall,  $T_w^{(\text{iso})}(t) \equiv 0$  and  $\rho_w^{(\text{iso})}(t)$  is treated unknown. For an adiabatic wall, both  $T_w^{(\text{ad})}(t)$  and  $\rho_w^{(\text{ad})}(t)$  should be determined. Considering a specular-wall setup, the probability perturbation function satisfies the symmetry condition

$$\phi(0, t, \xi_x > 0, \xi_y, \xi_z) = \phi(0, t, -\xi_x, \xi_y, \xi_z). \quad (9)$$

The diffuse (adiabatic or isothermal) and specular wall setups are subsequently analyzed in Secs. 3.1 and 3.2, respectively.

### 3.1 Diffuse wall

Considering a fully diffuse *adiabatic* wall, the solution for Eq. (5) subject to the initial condition (6) and boundary condition (8) is

$$\phi^{(\text{ad})}(x, t, \xi) = \begin{cases} \rho_{\text{in}}(x - \xi_x t) + T_{\text{in}}(x - \xi_x t)(\xi^2 - 3/2) & , \quad \xi_x \leq x/t \\ \rho_w^{(\text{ad})}(t - x/\xi_x) + T_w^{(\text{ad})}(t - x/\xi_x)(\xi^2 - 3/2) & , \quad \xi_x > x/t \end{cases} \quad (10)$$

separating, at location  $x$  and time  $t$ , between particles which have ( $\xi_x > x/t$ ) or have not ( $\xi_x \leq x/t$ ) hit the wall since the initial  $t = 0$  time. Here, the time-dependent wall functions  $\rho_w^{(\text{ad})}(t)$  and  $T_w^{(\text{ad})}(t)$  should be determined. To this end, we apply Eq. (4) and impose the linearized forms of the impermeability

$$u^{(\text{ad})}(0, t) = \frac{1}{\pi^{3/2}} \int_{-\infty}^{\infty} \xi_x \phi^{(\text{ad})}(0, t, \xi) \exp[-\xi^2] d\xi = 0 \quad (11)$$

and zero-heat-flux

$$q^{(\text{ad})}(0, t) = \frac{1}{2\pi^{3/2}} \int \xi_x \xi^2 \phi^{(\text{ad})}(0, t, \xi) \exp[-\xi^2] d\xi = 0 \quad (12)$$

conditions at the boundary. Substituting Eq. (10) into Eqs. (11) and (12), carrying out the  $\xi_y, \xi_z$  integrations, and making the change of variables  $s = -\xi_x t$ , yield the closed-form expressions for  $\rho_w^{(\text{ad})}(t)$  and  $T_w^{(\text{ad})}(t)$ ,

$$\begin{aligned} \rho_w^{(\text{ad})}(t) &= -\frac{1}{2t^2} \int_0^{\infty} s \left[ \left( \frac{s^2}{t^2} - 5 \right) \rho_{\text{in}}(s) + \left( \frac{s^4}{t^4} - \frac{11s^2}{2t^2} + \frac{7}{2} \right) T_{\text{in}}(s) \right] \exp \left[ -\frac{s^2}{t^2} \right] ds \quad \text{and} \\ T_w^{(\text{ad})}(t) &= \frac{1}{t^2} \int_0^{\infty} s \left[ \left( \frac{s^2}{t^2} - 1 \right) \rho_{\text{in}}(s) + \left( \frac{s^4}{t^4} - \frac{3s^2}{2t^2} + \frac{3}{2} \right) T_{\text{in}}(s) \right] \exp \left[ -\frac{s^2}{t^2} \right] ds, \end{aligned} \quad (13)$$

specifying their dependencies on the gas prescribed initial disturbances. Having fixed the solution for  $\phi(x, t, \xi)$ , appropriate quadratures over the velocity space yield expressions for the  $O(\varepsilon)$  density  $\rho^{(\text{ad})}(x, t)$ , normal velocity  $u^{(\text{ad})}(x, t)$ , pressure  $p^{(\text{ad})}(x, t)$  and temperature  $T^{(\text{ad})}(x, t)$  perturbations, as detailed in Appendix A.1.



Traversing to the case of a fully diffuse *isothermal* wall, the above formulation simplifies, as  $T_w^{(\text{iso})}(t) \equiv 0$ . The solution for Eq. (5) subject to the initial condition (6) and boundary condition (8) is then

$$\phi^{(\text{iso})}(x, t, \xi) = \begin{cases} \rho_{\text{in}}(x - \xi_x t) + T_{\text{in}}(x - \xi_x t)(\xi^2 - 3/2) & , \quad \xi_x \leq x/t \\ \rho_w^{(\text{iso})}(t - x/\xi_x) & , \quad \xi_x > x/t . \end{cases} \quad (14)$$

Prescribing the impermeability condition and omitting the adiabatic constraint at the surface, we obtain

$$\rho_w^{(\text{iso})}(t) = \frac{2}{t^2} \int_0^\infty s \left[ \rho_{\text{in}}(s) + T_{\text{in}}(s) \left( \frac{s^2}{t^2} - \frac{1}{2} \right) \right] \exp \left[ -\frac{s^2}{t^2} \right] ds. \quad (15)$$

The expressions for the  $O(\varepsilon)$  hydrodynamic perturbations then follow by replacing  $\rho_w^{(\text{ad})}(t)$  and  $T_w^{(\text{ad})}(t)$  in Eqs. (A1)-(A4) by  $\rho_w^{(\text{iso})}(t)$  and  $T_w^{(\text{iso})}(t) \equiv 0$ , respectively.

## 3.2 Specular wall

The specular wall setup may be analyzed by superposing the gas response to initial disturbances in the absence of a boundary [ $x \in (-\infty, \infty)$ ] with its symmetrical image about the surface location, such that the boundary condition (9) is identically satisfied. Making use of the linearized free-molecular solution in an unbounded domain [see Eqs. (5) and (6)],

$$\phi^{(\text{no-wall})}(x, t, \xi) = \phi_{\text{in}}(x - \xi_x t, \xi), \quad (16)$$

the probability perturbation function in the case of a specular wall configuration [ $x \in [0, \infty)$ ] is given by

$$\phi^{(\text{spec})}(x, t, \xi_x, \xi_y, \xi_z) = \begin{cases} \phi_{\text{in}}(x - \xi_x t, \xi_x, \xi_y, \xi_z) & , \quad \xi_x \leq x/t \\ \phi_{\text{in}}(-x + \xi_x t, -\xi_x, \xi_y, \xi_z) & , \quad \xi_x > x/t. \end{cases} \quad (17)$$

Substituting Eq. (17) into Eq. (4), the expressions for the hydrodynamic fields follow by appropriate quadratures over the velocity space, as documented in Appendix A.2.

Observing the differences between the diffuse and specular wall descriptions [cf. Eqs. (10), (14) and (17)], it is expected that the change in wall conditions affects the propagation of initial disturbances in the gas. The significance of these differences and their comparison with the propagation of flow non-uniformities in an infinite domain are discussed in Sec. 6.

## 4 Near-continuum conditions

The problem at small Knudsen numbers or relatively long times (i.e.,  $t/\text{Kn} \gg 1$ ) is next analyzed using a ‘slip-flow’ continuum-limit model in Sec. 4.1, consisting of the continuum Navier-Stokes-Fourier (NSF) balance equations and respective wall conditions. The regularized thirteen moment (R13) scheme is applied in Sec. 4.2 in an effort to capture the system behavior at conditions that further depart from continuum. The NSF and R13 problems for a fully-diffuse wall are formulated in Secs. 4.1 and 4.2, respectively, and the case of a specular surface is analyzed in Sec. 4.3.

### 4.1 The continuum limit

To consider the problem at continuum-limit conditions, we make use of the NSF equations, supplemented by a set of initial and wall impermeability and thermal conditions. Adopting the scaling introduced in Sec. 2, the model consists of the unsteady one-dimensional linearized equations of continuity,

$$\frac{\partial \rho}{\partial t} + \frac{\partial u}{\partial x} = 0, \quad (18)$$

$x$ -momentum,

$$\frac{\partial u}{\partial t} = -\frac{1}{2} \left( \frac{\partial \rho}{\partial x} + \frac{\partial T}{\partial x} \right) + \frac{4}{3} \widetilde{\text{Kn}} \frac{\partial^2 u}{\partial x^2}, \quad (19)$$

and energy,

$$\frac{\partial T}{\partial t} = -\frac{\gamma \widetilde{\text{Kn}}}{\text{Pr}} \frac{\partial^2 T}{\partial x^2} - (\gamma - 1) \frac{\partial u}{\partial x}, \quad (20)$$

where the linearized form of the equation of state in an ideal gas,  $p = \rho + T$ , has been applied. In Eqs. (19)-(20),

$$\widetilde{\text{Kn}} = \frac{\nu_0^*}{U_{\text{th}}^* l^*} \text{Kn} \quad (21)$$

is the viscosity-based Knudsen number, where  $\nu_0^*$  denotes the gas kinematic viscosity at the reference temperature  $T_0^*$ . Considering the gas kinetic model of *Maxwell molecules* implies that  $l^* = \nu_0^*/U_{\text{th}}^*$ , where  $\nu_0^*$  is linearly proportional to the reference gas temperature  $T_0^*$  [29]. Consequently,

$$\widetilde{\text{Kn}} = \text{Kn} = \nu_0^*/(U_{\text{th}}^* L^*).$$

Also appearing in Eq. (20) are the gas Prandtl number  $Pr$  and ratio of specific heats  $\gamma$ , which equal, for an ideal monatomic gas,  $2/3$  and  $5/3$ , respectively. In line with the statement of the problem, the equations are supplemented by the initial conditions [cf. Eq. (1)]

$$\rho(x, 0) = \rho_{\text{in}}(x), \quad u(x, 0) = 0 \quad \text{and} \quad T(x, 0) = T_{\text{in}}(x), \quad (22)$$

together with the impermeability,

$$u(0, t) = 0, \quad (23)$$

and a thermal condition at the wall. For an adiabatic surface, this condition is given by

$$\left. \frac{\partial T}{\partial x} \right|_{(0,t)} = 0, \quad (24)$$

in accordance with the linearized form of the Fourier law of heat conduction. For an isothermal wall, a first-order temperature jump condition,

$$T(0, t) = -\sqrt{\pi}\tau_q q(0, t) - \frac{1}{2}\tau_\sigma \sigma(0, t), \quad (25)$$

is applied, where

$$q(0, t) = -\frac{15}{8}\text{Kn} \left. \frac{\partial T}{\partial x} \right|_{(0,t)} \quad \text{and} \quad \sigma(0, t) = -\frac{4}{3}\text{Kn} \left. \frac{\partial u}{\partial x} \right|_{(0,t)}$$

are the NSF normal heat-flux and deviatoric stress (with the latter scaled by  $\rho_0^* U_{\text{th}}^{*2}$ ) on the wall, respectively. The jump coefficients  $\tau_q$  and  $\tau_\sigma$  generally depend on the type of molecular interaction (with their values derived in Ref. [31] for hard-sphere and BGK models), yet were set here to unity to comply with the higher-order jump conditions applied in Eq. (32) for Maxwell molecules [32]. Far-field ( $x \rightarrow \infty$ ) decay conditions are additionally imposed on all perturbations.

## 4.2 Regularized moment equations

While the continuum-limit model is expected to hold at sufficiently large values of  $t/\text{Kn}$ , it is desirable to apply a higher-order scheme to capture the gas state at somewhat shorter times. Towards this end, we make use of the R13 scheme [33, 34], which has been previously applied to analyze steady [35] and unsteady (e.g., Refs. [13, 36]) flow problems. The scheme has been

derived primarily for a Maxwell-type model of molecular interaction, where the three-dimensional formulation consists of balances for the gas scalar density and temperature, the vectors of velocity and heat-flux, and the stress tensor. Higher order moments are coupled to the system through a Chapman-Enskog-type expansion of the probability density function in the kinetic Boltzmann equation. Assuming, as above, a linearized unsteady one-dimensional setup, the governing equations consist of the continuity equation (18), together with the hydrodynamic balances of  $x$ -momentum,

$$\frac{\partial u}{\partial t} = -\frac{1}{2} \left( \frac{\partial \rho}{\partial x} + \frac{\partial T}{\partial x} \right) - \frac{\partial \sigma}{\partial x} \quad (26)$$

and energy,

$$\frac{\partial T}{\partial t} = -\frac{4}{3} \frac{\partial q}{\partial x} - \frac{2}{3} \frac{\partial u}{\partial x}, \quad (27)$$

equations. The normal stress  $\sigma(x, t)$  and heat-flux  $q(x, t)$  appearing in Eqs. (26) and (27) satisfy the closure relations

$$\frac{\partial \sigma}{\partial t} = -\frac{8}{15} \frac{\partial q}{\partial x} - \frac{2}{3} \frac{\partial u}{\partial x} + \frac{6}{5} \text{Kn} \frac{\partial^2 \sigma}{\partial x^2} - \frac{1}{2 \text{Kn}} \sigma \quad (28)$$

and

$$\frac{\partial q}{\partial t} = -\frac{5}{8} \frac{\partial T}{\partial x} - \frac{1}{2} \frac{\partial \sigma}{\partial x} + \frac{18}{5} \text{Kn} \frac{\partial^2 q}{\partial x^2} - \frac{1}{3 \text{Kn}} q, \quad (29)$$

obtained with  $\gamma = 5/3$  and  $\text{Pr} = 2/3$ . In accordance with the problem statement, the system of equations is subject to the set of initial conditions

$$\rho(x, 0) = \rho_{\text{in}}(x), \quad u(x, 0) = 0, \quad T(x, 0) = T_{\text{in}}(x), \quad \sigma(x, 0) = 0, \quad q(x, 0) = 0 \quad (30)$$

together with respective wall-surface and far-field decay conditions. The former include the impermeability condition (23) combined with thermal and high-order moment balances at  $x = 0$ .

The conditions differ between an adiabatic wall,

$$q(0, t) = 0 \quad \text{and} \quad \left[ \frac{15}{2} \sigma - 6 \text{Kn} \left( \sqrt{\pi} \frac{\partial \sigma}{\partial x} + \frac{4}{7} \frac{\partial q}{\partial x} \right) \right]_{(0,t)} = 0, \quad (31)$$

and an isothermal wall,

$$\left[ T + \frac{1}{2} \sigma + \sqrt{\pi} q - \frac{96}{35} \text{Kn} \frac{\partial q}{\partial x} \right]_{(0,t)} = 0 \quad \text{and} \quad \left[ T - 7 \sigma + 6 \text{Kn} \left( \sqrt{\pi} \frac{\partial \sigma}{\partial x} + \frac{4}{35} \frac{\partial q}{\partial x} \right) \right]_{(0,t)} = 0. \quad (32)$$

In Eq. (32), the left-hand equation represents a temperature-jump wall condition. This condition degenerates into Eq. (25) for  $\text{Kn} \ll 1$  [omitting  $O(\text{Kn}^2)$  terms]. The right-hand equation is a

linearized reduction of the high-order moment condition obtained by Gu and Emerson [32] and applied by Struchtrup [13] in a one-dimensional setup. As expected, a temperature jump condition is missing from the adiabatic-wall balances in Eq. (31), and replaced by a vanishing heat-flux condition. The right-hand balance is derived by eliminating the unknown wall temperature perturbation from Eqs. (30) and (31) in Gu and Emerson [32], or, equivalently, from Eq. (9) in Ref. [13].

### 4.3 Analysis

#### 4.3.1 Diffuse wall

Different from the free-molecular regime considered in Sec. 3, the near-continuum problems for a fully-diffuse wall formulated in Secs. 4.1 and 4.2 are not amenable to a closed-form solution. Hence, a finite difference scheme was applied. To evaluate the  $x$ -derivatives at each time-step, the problems were discretized in the  $x$ -direction based on a central-difference second-order approximation. A far-field decay condition was imposed at a finite, yet sufficiently far location, such that the signal does not reach the outer boundary within the simulated time period. Time integration was followed using a Matlab ODE solver. While requiring some minimal computation effort, these calculations were far less demanding than their counterpart Monte Carlo simulations (see Sec. 5), particularly at increasingly small Knudsen numbers, where DSMC computations become prohibitively expensive.

#### 4.3.2 Specular wall

In similar to Sec. 3.2, the near-continuum gas response for a perfectly specular wall may be obtained by superposing the gas evolution in the absence of a boundary with its symmetrical image about the surface location. In terms of the hydrodynamic problem formulation, this is equivalent to imposing the vanishing of all odd moments of the probability density function (including the normal velocity, normal heat-flux and higher-order non-even moments) at the wall, whereas all even moments are symmetric about  $x = 0$ . Notably, these conditions are

identical to the adiabatic-wall conditions in the continuum NSF description [cf. Eqs. (23) and (24)], and it is therefore expected that the gas behavior in both systems is indistinguishable at  $t/\text{Kn} \gg 1$ . Discrepancies between the specular- and isothermal-wall responses are expected in all near-continuum flow regimes, and should additionally become observable with decreasing  $t/\text{Kn}$  (either by decreasing  $t$  or increasing gas rarefaction) between specular- and adiabatic-wall setups. This is manifested through the non-symmetrical form of the high-order wall condition in Eq. (31), which, in a formulation of the counterpart R13 specular-wall-containing problem, should be replaced by the condition  $[\partial\sigma/\partial x]_{(0,t)} = 0$ . The deviations between the specular and diffuse-adiabatic systems response become larger with increasing rarefaction, due to the increasing effects of high-order moments, and maximize at free-molecular conditions, as demonstrated in Sec. 6 (see Figs. 2 and 7)

To derive the specular-wall system response, we start by analyzing the gas evolution in the non-confined setup, and focus initially on the continuum NSF limit. Referring to the scheme presented in Sec. 4.1, the problem consists of Eqs. (18)-(20) combined with the initial conditions (22) and far-field decay conditions. In the present infinite  $x$ -domain, it is convenient to apply the Fourier  $x$ -transform,

$$\overline{G}(\lambda, t) = \int_{-\infty}^{\infty} G^{(\text{no-wall})}(x, t) \exp[-i\lambda x] dx, \quad (33)$$

where  $\overline{G} = \{\overline{\rho}, \overline{u}, \overline{T}\}$ , to the problem. This yields the system of transformed ordinary equations

$$\overline{\rho}' + i\lambda\overline{u} = 0, \quad \overline{u}' = -\frac{i\lambda}{2}(\overline{\rho} + \overline{T}) - \frac{4\text{Kn}}{3}\lambda^2\overline{u} \quad \text{and} \quad \overline{T}' = -\frac{\gamma\text{Kn}}{\text{Pr}}\lambda^2\overline{T} - i\lambda(\gamma - 1)\overline{u}, \quad (34)$$

where primes denote time differentiations and the Maxwell-molecules substitution  $\widetilde{\text{Kn}} = \text{Kn}$  has been made. The system is accompanied by the transformed initial conditions

$$\overline{\rho}(\lambda, 0) = \overline{\rho}_{\text{in}}(\lambda), \quad \overline{u}(\lambda, 0) = 0 \quad \text{and} \quad \overline{T}(\lambda, 0) = \overline{T}_{\text{in}}(\lambda) \quad (35)$$

in the  $(\lambda, t)$  plane. Substituting the above-stated  $\gamma = 5/3$  and  $\text{Pr} = 2/3$  values and eliminating  $\overline{u}$  and  $\overline{\rho}$  through

$$\overline{u} = \frac{3i}{2\lambda} \left( \overline{T}' + \frac{5}{2}\lambda^2\text{Kn}\overline{T} \right) \quad \text{and} \quad \overline{\rho} = -\frac{1}{\lambda^2} \left[ 3\overline{T}'' + \frac{23}{2}\lambda^2\text{Kn}\overline{T}' + \lambda^2(1 + 10\lambda^2\text{Kn}^2)\overline{T} \right], \quad (36)$$

we obtain a single equation for  $\bar{T}$ ,

$$\bar{T}''' + \frac{23}{6}\text{Kn}\lambda^2\bar{T}'' + \frac{5}{6}\lambda^2(1 + 4\lambda^2\text{Kn}^2)\bar{T}' + \frac{5}{4}\lambda^4\text{Kn}\bar{T} = 0. \quad (37)$$

The general solution for the transformed temperature perturbation is then

$$\bar{T}(t, \lambda) = A_0(\lambda)e^{r_0(\lambda)t} + A_+(\lambda)e^{r_+(\lambda)t} + A_-(\lambda)e^{r_-(\lambda)t}, \quad (38)$$

where  $r_0(\lambda)$  and  $r_{\pm}(\lambda)$  are the roots of the characteristic polynomial of Eq. (37). Evaluating these roots in the limit  $\text{Kn} \ll 1$  and omitting  $O(\text{Kn}^2)$  terms we obtain

$$r_0(\lambda) \approx -\frac{3}{2}\lambda^2\text{Kn} \quad \text{and} \quad r_{\pm}(\lambda) \approx \pm\sqrt{\frac{5}{6}}i\lambda - \frac{7}{6}\lambda^2\text{Kn}. \quad (39)$$

The values of the coefficients  $A_0(\lambda)$  and  $A_{\pm}(\lambda)$  in the particular solution are fixed by substituting Eq. (38) together with Eq. (36) into Eq. (35). Having determined  $\bar{T}(\lambda, t)$ ,  $\bar{\rho}(\lambda, t)$  and  $\bar{u}(\lambda, t)$ , the system response in the physical  $(x, t)$  plane is evaluated by taking the inverse transform

$$G^{(\text{no-wall})}(x, t) = \frac{1}{2\pi} \int_{-\infty}^{\infty} \bar{G}(x, t) \exp[i\lambda x] d\lambda. \quad (40)$$

A similar procedure, not detailed here for brevity, is followed to calculate the counterpart specular-wall R13 gas description. Here, based on the analysis in Sec. 4.2, a fifth-order system of equations is obtained. Since the roots of the characteristic polynomial cannot be estimated analytically, numerical evaluation is carried out. The solution is then given by

$$\bar{G}(\lambda, t) = \sum_{n=1}^5 A_{G_n}(\lambda) e^{r_n(\lambda)t}, \quad (41)$$

where  $\bar{G} = \{\bar{\rho}, \bar{u}, \bar{T}, \bar{\sigma}, \bar{q}\}$ ,  $r_n(\lambda)$  mark the roots of the characteristic polynomial, and  $A_{G_n}(\lambda)$  are determined via imposition of the initial conditions [transformed form of Eq. (30)]. Numerical investigation of  $r_n(\lambda)$  indicates that  $r_{1,2,3}(\lambda)$  converge to their NSF  $r_0$  and  $r_{\pm}$  counterparts at  $\text{Kn} \ll 1$  [see Eq. (39)]. The remaining Fourier-transformed modes are governed by the roots

$$r_4 \approx -\frac{1}{2\text{Kn}} \quad \text{and} \quad r_5 \approx -\frac{1}{3\text{Kn}}, \quad (42)$$

which are independent of  $\lambda$ . At  $\text{Kn} \ll 1$ , these modes should approximate the initial Knudsen-layer behaviour of the gas, inevitably missing in the NSF description. As in the NSF approximation,

once the transformed  $\overline{G}(\lambda, t)$  fields are determined, the solution is transformed back to the  $(x, t)$  plane using Eq (40).

Having obtained the unbounded gas response, the procedure for calculating the specular-wall system solution  $G^{(\text{spec})}(x, t)$  is carried out by superposing  $G^{(\text{no-wall})}(x, t)$  with its symmetrical image about  $x = 0$ . This ensures the vanishing of all odd hydrodynamic moments at  $x = 0$ , as required by the specular boundary condition. Notably, the above derivation tacitly assumes that the initial system perturbation (1) is localized about  $x = 1$  (or  $x^* = L^*$  in dimensional notation), so that its superposition with its  $x < 0$  image at time  $t = 0$  agrees with the physical initial conditions within  $x \geq 0$ . This restriction is satisfied in our specific choice for the initial system state [see Eq. (47)], where we focus on the gas response to an initially space-confined (localized) excitation. For later reference we note that, while the NSF and R13 schemes expectedly yield identical results at late times ( $t/\text{Kn} \gg 1$ ), the latter should better approximate the system behavior at earlier times. This will be illustrated in Sec. 6 (see Fig. 6).

## 5 Numerical scheme: DSMC method

The DSMC method, initially proposed by Bird [37], is a stochastic particle method commonly applied to the analysis of gas flows at non-continuum conditions. In the present work, we make use of the DSMC scheme to validate the analytical ballistic- and continuum-limit solutions presented in Secs. 3 and 4. We accordingly adopt Bird's algorithm, together with the Variable Hard Sphere (VHS) model of molecular interaction [37], to simulate the gas state. To enable comparison between the DSMC and continuum solutions for Maxwell molecules, the molecular collision cross section is defined as detailed in Ref. [36] (see Sec. 5 therein). In line with the problem formulation, the wall surface is assumed either specular or fully diffuse, with prescribed temperature or heat-flux. To apply the latter, the boundary temperature is treated as unknown, and a modification of the conventional numerical scheme is required. This is carried out based on recent contributions by the authors [36, 38–41], where a non-iterative algorithm for the imposition of a heat-flux condition has been suggested and tested. For completeness, the algorithm is repeated here.



We consider the distribution of the (dimensional) normal and tangential velocity components for the wall-reflected molecules at the  $i$ -th time step,

$$v_{\perp}^{*i} = \frac{1}{\beta_w^{*i}} \sqrt{-\ln(R_U)} \quad \text{and} \quad v_{\parallel}^{*i} = \frac{1}{\sqrt{2} \beta_w^{*i}} R_G, \quad (43)$$

respectively. In Eq. (43),  $R_U \in [0, 1]$  and  $R_G \in (-\infty, \infty)$  are uniformly- and Gaussian-distributed random numbers, and  $\beta_w^{*i} = \sqrt{1/2\mathcal{R}^*T_w^{*i}}$ . When assigning a heat-flux condition, the value of  $\beta_w^{*i}$  is *a priori* unknown, and should be determined at every time step. Assuming a fully diffuse boundary, the total mass and thermal energy fluxes of the molecules reflected at the surface are given by

$$\mathcal{M}_{\text{out}}^{*i} = \frac{\rho_w^{*i}}{2\beta_w^{*i} \sqrt{\pi}} \quad \text{and} \quad \mathcal{H}_{\text{out}}^{*i} = \frac{\rho_w^{*i}}{2(\beta_w^{*i})^3 \sqrt{\pi}}, \quad (44)$$

respectively. Applying the conservations of mass,  $\mathcal{M}_{\text{out}}^{*i} = \mathcal{M}_{\text{in}}^{*i}$ , and thermal energy,  $\mathcal{H}_{\text{out}}^{*i} = \mathcal{H}_{\text{in}}^{*i}$ , at the aforementioned *adiabtic* wall, we obtain

$$\beta_w^{*i} = \sqrt{\frac{\mathcal{M}_{\text{in}}^{*i}}{\mathcal{H}_{\text{in}}^{*i}}}, \quad (45)$$

where  $\mathcal{M}_{\text{in}}^{*i}$  and  $\mathcal{H}_{\text{in}}^{*i}$  are computed at each time step via

$$\mathcal{M}_{\text{in}}^{*i} = \frac{N}{\Delta t^*} \quad \text{and} \quad \mathcal{H}_{\text{in}}^{*i} = \frac{1}{2\Delta t^*} \sum_{j=1}^N \left[ (\xi_x^{*i,j})^2 + (\xi_y^{*i,j})^2 + (\xi_z^{*i,j})^2 \right]. \quad (46)$$

In Eq. (46), summation is carried over all  $j = 1, \dots, N$  particles that have collided with the boundary during the  $\Delta t^*$  time interval. Having determined  $\mathcal{M}_{\text{in}}^{*i}$  and  $\mathcal{H}_{\text{in}}^{*i}$ ,  $\beta_w^{*i}$  is obtained using Eq. (45). Each of the reflected particles is then assigned a velocity according to Eq. (43), and the simulation is followed to the next time step.

The computation was followed in time, starting at  $t^* = 0$  and terminating at  $t_{\text{sim}}^* = 4L^*/U_{\text{th}}^*$  (which proved sufficient for the investigation of the effect of wall reflection on system relaxation). At these times, the size of the computational domain was set such that the signal does not reach (and is therefore not affected by) a virtual outer boundary placed at  $x_{\text{sim}}^* \approx (10 \div 15)L^*$ . The  $[0, x_{\text{sim}}^*]$   $x^*$ -domain was divided into  $100 \div 200$  cells, and an additional division of each cell into collisional subcells was carried to comply with the mean-free-path limitations. Specifically, the width of the subcells was set to  $l^*/4$  and the magnitude of time increment was set to  $1/4 \times l^*/U_{\text{th}}^*$ . A typical run

consisted of  $\approx 10^7$  particles, where  $\approx 1500$  realizations were carried out to sufficiently reduce the numerical noise. Each simulation lasted several hours using a ten core Intel i7-6950 machine. In line with the linearized problem formulation, a value of  $\varepsilon = 0.05$  was taken, for which non-linear effects are negligible.

## 6 Results

Applying the above analyses, our results may be presented for arbitrary choices of the gas initial density and temperature perturbations,  $\rho_{\text{in}}(x)$  and  $T_{\text{in}}(x)$ . Yet, in what follows we limit our discussion to setups where only local fluid heating is imposed, to analyze the gas and wall responses to space-confined thermal disturbances. This may resemble processes of acoustic propagation encountered in micro-scale heat transfer applications, mentioned in the Introduction [21, 22]. Specifically, we consider the initial distributions

$$\rho_{\text{in}}(x) = 0 \quad \text{and} \quad T_{\text{in}}(x) = \exp\left[-\alpha(x-1)^2\right], \quad (47)$$

marking a Gaussian temperature disturbance peaked at  $x = 1$ . A value of  $\alpha = 20$  ( $\gg 1$ ) is taken to mimic a localized initial perturbation that decays sharply about  $x = 1$ . This enables the inspection of the entire wall effect (vs. the non-confined configuration), which does not impact the system evolution at  $t \rightarrow 0$ , and becomes dominant with increasing time. The Knudsen number ( $\text{Kn} = l^*/L^*$ ) is subsequently interpreted as the inverse of the distance between the peak source location and the wall in mean-free-path units, thus characterizing the flow regime (free-molecular, intermediate or near-continuum) expected at times  $t \sim O(1)$  of intense gas-wall interaction. In Secs. 6.1 and 6.2, the free-molecular ( $t/\text{Kn} \ll 1$ ) and near-continuum ( $t/\text{Kn} \gg 1$ ) gas responses are described. The effect of the solid boundary is discussed, and the occurrence of intermediate-flow conditions [at  $t/\text{Kn} \sim O(1)$ ] is characterized through comparisons with DSMC predictions. Sec. 6.3 analyses the unsteady force exerted on the wall through flow-surface interactions and further quantitates the impact of boundary conditions on the intensity of acoustic reflection.

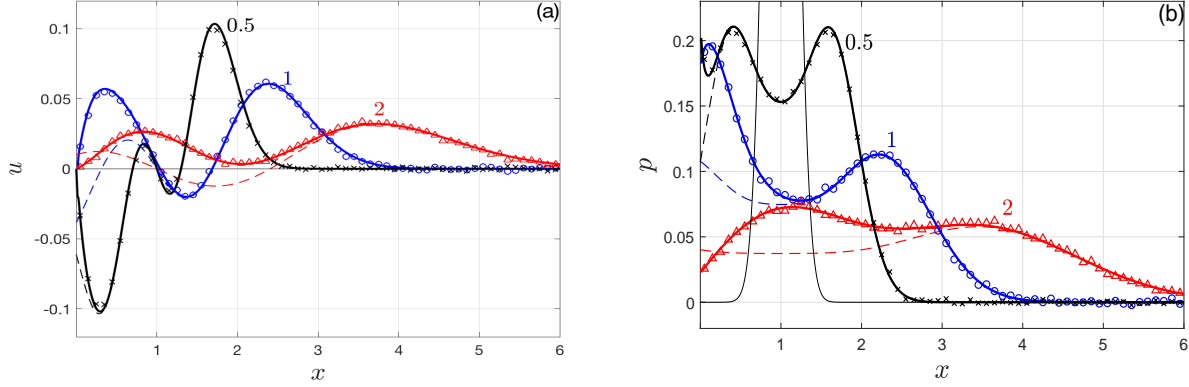


Figure 1: Time snapshots (at the indicated times  $t = 0.5, 1$  and  $2$ ) of the (a) normal velocity and (b) acoustic pressure for an isothermal-wall setup at free-molecular (solid curves) and  $\text{Kn} = 5$  (symbols, DSMC predictions) conditions. The thin dashed lines show counterpart free-molecular results in a non-confined setup. The thin solid curves depict the initial ( $t = 0$ ) distributions of the velocity and acoustic pressure, with the latter shown only in part for better clarity of the results at later times.

## 6.1 Free-molecular limit

For the initial distributions specified in Eq. (47), the free-molecular analysis in Sec. 3 may be followed slightly further by obtaining closed-form formulae for the wall functions  $\rho_w^{(\text{ad})}(t)$  and  $T_w^{(\text{ad})}(t)$  in the adiabatic-wall system, as well as for  $\rho_w^{(\text{iso})}(t)$  in the isothermal-boundary setup. Substituting Eq. (47) into Eqs. (13) and (14) and carrying out the required integrations, the expressions obtained are specified in Appendix B. Apart from simplifying the evaluation of the hydrodynamic fields in Appendix A.1, these expressions turn useful in the discussion of the unsteady force exerted on the boundary in Sec. 6.3.

To illustrate the free-molecular flow field, Figure 1 shows time snapshots of the normal velocity and acoustic pressure for an isothermal-wall setup at  $\text{Kn} \rightarrow \infty$  ( $t/\text{Kn} \rightarrow 0$ ) based on the solution derived in Sec. 3. The results are compared with DSMC predictions at  $\text{Kn} = 5$ , which, at the indicated times  $t = 0.5, 1$  and  $2$ , correspond to  $t/\text{Kn} = 0.125, 0.2$  and  $0.4$ , respectively.

The agreement between the results is very good in all cases, supporting the validity of the free-molecular description at short times.

Inspecting the velocity and pressure signals at  $t = 0.5$ , we observe that they are nearly identical with their non-confined setup counterparts, marked by the dashed curves. Indeed, at this early time, the symmetry-breaking effect of the wall is minor (and observed only in its very vicinity), and the disturbances propagate nearly symmetrically (for the even moments), or anti-symmetrically (for the odd moments), about  $x = 1$ , the location of maximum initial perturbation. With increasing time, the wall impact forms as a reflected wave propagating away from the surface. The extent of the  $x$ -interval affected by the wall, shown by the  $x$ -interval where the confined and non-confined responses differ, increases with  $t$ , covering  $0 < x \lesssim 3.5$  at the latest time  $t = 2$  presented.

To investigate the effect of surface conditions on sound propagation at large rarefaction rates, Figure 2 presents a comparison between the acoustic pressure for specular, adiabatic and isothermal wall systems. Figs. 2a and 2b describe the  $x$ -variations of the acoustic signals at times  $t = 1$  and  $t = 2$ , respectively. Fig. 2c shows the time-variation of the pressure perturbation at a fixed  $x = 0.6$  location. The value of the pressure at  $t = 0$  in Fig. 2c agrees with its initially imposed  $p(0.6, 0) = \rho_{\text{in}}(0.6) + T_{\text{in}}(0.6) \approx 0.041$  level, in agreement with Eq. (47) and the linearized equation of state. The isothermal-wall results in Figs. 2a and 2b are identical with those shown in Fig. 1, for reference. Close agreement is noted, as in Fig. 1, between the  $\text{Kn} = 5$  DSMC and free-molecular predictions in the specular- and adiabatic-wall systems.

Comparing between the signals in the three setups, we observe that the pressure amplitude in the isothermal-wall case is consistently lower than in the specular- and adiabatic-wall configurations. Indeed, different from the latter two setups, the isothermal wall absorbs thermal energy from the impinging wave, thus emitting an overall weaker acoustic disturbance. This suggests that the imposition of a monitored (time-dependent) heat-flux boundary condition may be efficient in reducing the wall reflection. A similar approach has been applied in a different context to minimize the vibroacoustic noise of a mechanically-actuated surface [36, 38, 41, 42]. Ideally, an acoustically cloaked system should recapture the pressure signal marked by the dashed curves in Fig. 2, which deflect from the surface-confined signals at  $(x, t)$  combinations where the

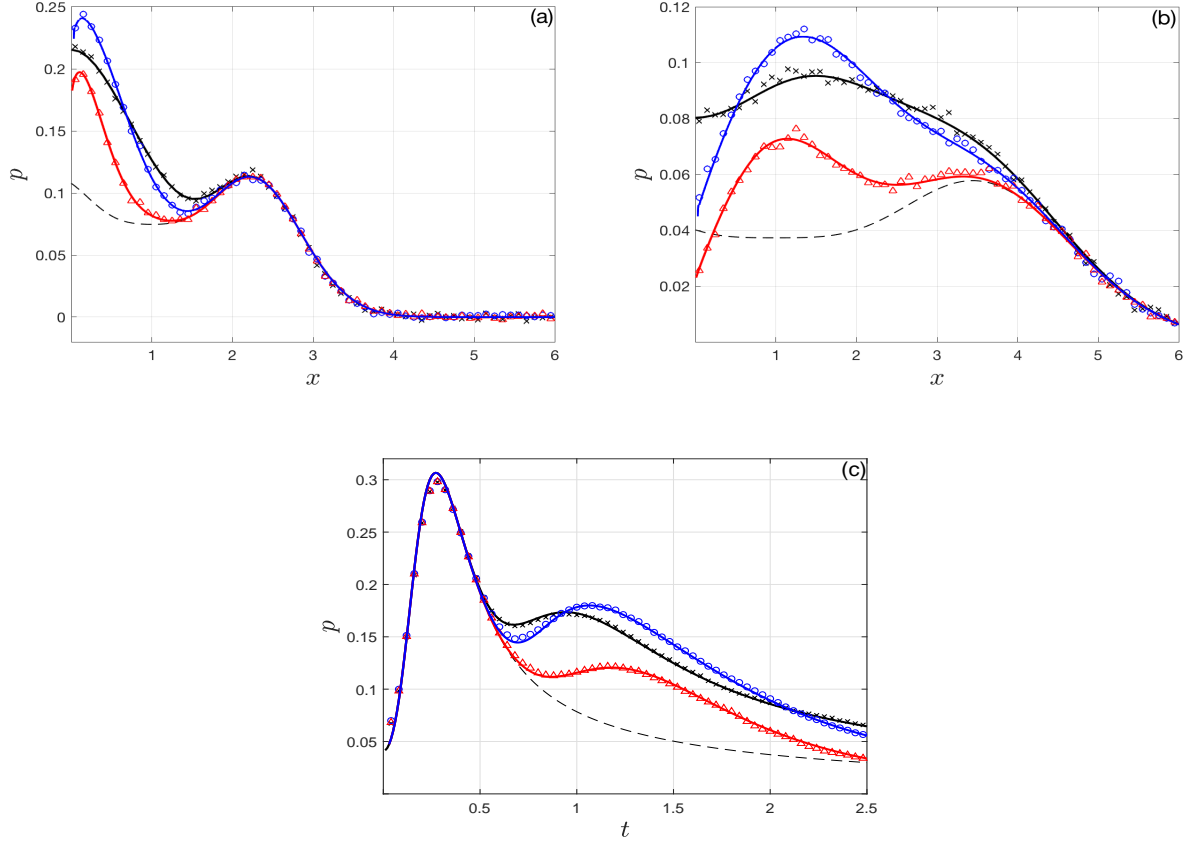


Figure 2: Effect of the wall boundary condition on the acoustic pressure at large rarefaction rates: (a,b) time snapshots at (a)  $t = 1$  and (b)  $t = 2$ ; (c) time variation at a fixed  $x = 0.6$  location. The solid curves present the free-molecular solution and the symbols mark DSMC predictions at  $\text{Kn} = 5$ . The black, blue and red notations show results for specular, adiabatic and isothermal wall configurations, respectively. The thin dashed lines depict counterpart results in a non-confined setup.

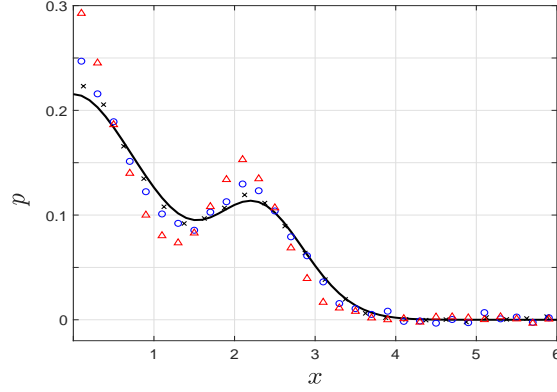


Figure 3: Breakdown of the free-molecular description with increasing  $t/\text{Kn}$ :  $x$ -variations of the acoustic pressure at  $t = 1$  in the free-molecular limit (solid line) compared with DSMC results at  $\text{Kn} = 1$  (crosses),  $0.5$  (circles) and  $0.2$  (triangles) for a specular wall setup.

boundary-reflected signal has reached the point of reference. In Fig. 2c, this occurs for  $t \gtrsim 0.65$ , after the disturbance, initially propagating symmetrically about  $x = 1$  in the negative and positive  $x$ -directions, has been reflected from the wall and returned to  $x = 0.6$ .

The breakdown of the free-molecular description is considered in Fig. 3, where the variation of the acoustic pressure at time  $t = 1$  is compared between collisionless and DSMC results at finite Knudsen numbers. The figure shows DSMC predictions at  $\text{Kn} = 1, 0.5$  and  $0.2$ , which correspond to  $t/\text{Kn} = 1, 2$  and  $5$ , respectively, at  $t = 1$ . Notably, The free-molecular results match well with simulations up to times  $t/\text{Kn} = 1$ , and show reasonable agreement even at  $t/\text{Kn} = 2$ . The effect of molecular collisions becomes non-negligible at later times, and dominates the near-continuum regime discussed below.

## 6.2 Near-continuum conditions

Considering the system response at long times ( $t/\text{Kn} \gg 1$ ), we first note that the NSF solution in the non-confined setup may be approximated in a closed form for the initial conditions specified in Eq. (47). To this end,  $A_0(\lambda)$ ,  $A_+(\lambda)$  and  $A_-(\lambda)$  in Eq. (38) may be evaluated for  $\text{Kn} \ll 1$ , and the

inverse Fourier transform (40) can be applied to yield

$$\begin{aligned}
T^{(\text{no-wall})}(x, t) \approx & \frac{1}{5} \left\{ \frac{3}{\sqrt{1 + 6\alpha\text{Kn}t}} \exp \left[ -\frac{\alpha(x-1)^2}{1 + 6\alpha\text{Kn}t} \right] \right. \\
& + \frac{1 - \alpha\text{Kn} \left[ t + \frac{17}{3} \sqrt{\frac{6}{5}}(x-1) \right]}{\left( 1 + \frac{14}{3}\alpha\text{Kn}t \right)^{3/2}} \exp \left[ -\frac{\alpha \left( x-1 + \sqrt{\frac{5}{6}}t \right)^2}{1 + \frac{14}{3}\alpha\text{Kn}t} \right] + \\
& \left. \frac{1 - \alpha\text{Kn} \left[ t - \frac{17}{3} \sqrt{\frac{6}{5}}(x-1) \right]}{\left( 1 + \frac{14}{3}\alpha\text{Kn}t \right)^{3/2}} \exp \left[ -\frac{\alpha \left( x-1 - \sqrt{\frac{5}{6}}t \right)^2}{1 + \frac{14}{3}\alpha\text{Kn}t} \right] \right\} \quad (48)
\end{aligned}$$

for the temperature perturbation in the absence of a wall. Inspecting Eq. (48), it is observed that the gas response (which is qualitatively similar in all other hydrodynamic fields) combines one diffusive mode and two propagating waves spreading symmetrically about  $x = 1$  in the positive and negative  $x$ -directions. The  $\sqrt{5/6}$  factor multiplying the time (or its inverse multiplying the position) stems from the ratio between the wave phase velocity in the continuum ( $c_0^* = \sqrt{\gamma\mathcal{R}^*T_0^*}$ ) and free-molecular ( $U_{\text{th}}^* = \sqrt{2\mathcal{R}^*T_0^*}$ ) limits, indicating a slower propagation speed in the former. The system response in the case of a specular wall setup is obtained by superposing  $T^{(\text{no-wall})}(x, t)$  in Eq. (48) with its symmetric image about  $x = 0$ , yielding a signal combined of three propagating modes (omitting the wave initiated at the image location  $x = -1$  and propagating in the negative  $x$ -direction) and two diffusive modes. As noted in the beginning of Sec. 4.3.2, the above specular-wall response in the NSF limit should be identical with the counterpart adiabatic-wall system behavior.

Figure 4 presents time snapshots of the normal velocity and acoustic pressure for an isothermal-wall setup with  $\text{Kn} = 0.02$ . A comparison is made between NSF-based and DSMC predictions, showing a very good agreement at the presented times  $t = 0.5, 1$  and  $2$ , corresponding to  $t/\text{Kn} = 25, 50$  and  $100$ , respectively. The early-time ( $t = 0.5$ ) signal is fully symmetrical about  $x = 1$ , and is indiscernible from its counterpart non-confined wave, as the effect of wall reflection is negligible at this time. The continuum-limit solution at later (after wall reflection) times is characterized by distinct peaked waves that propagate away from the surface while gradually decaying. This is qualitatively different from the free-molecular system response, where the initial disturbance is quickly spreading and decaying at a higher rate, forming a weaker signal at

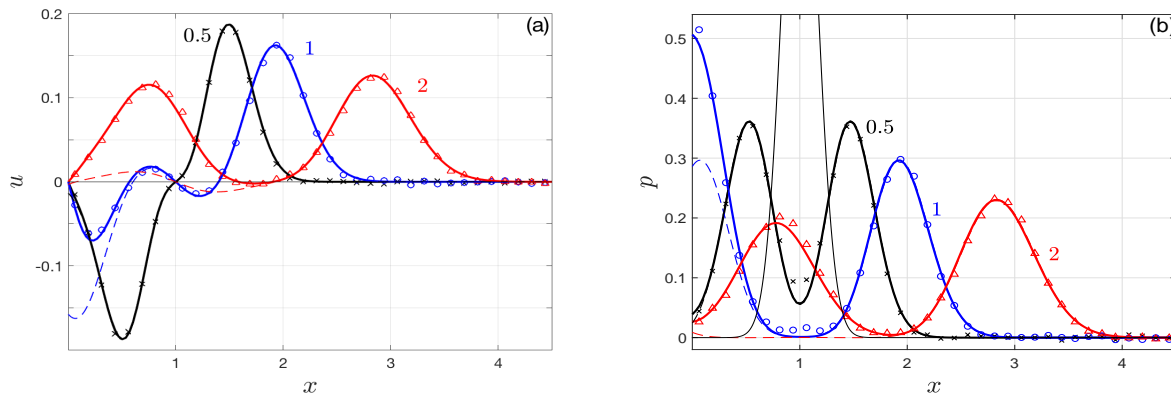


Figure 4: Time snapshots (at the indicated times  $t = 0.5, 1$  and  $2$ ) of the (a) normal velocity and (b) acoustic pressure for an isothermal-wall setup with  $\text{Kn} = 0.02$ . The solid curves and symbols compare between NSF and DSMC predictions, respectively. The thin dashed lines show counterpart NSF results in a non-confined setup. The thin solid curves depict the initial ( $t = 0$ ) distributions of the velocity and acoustic pressure, with the latter shown only in part for better clarity of the results at later times.



a given time (cf. the pressure amplitudes in Figs. 1b and 4b). Indeed, with decreasing  $\text{Kn} \rightarrow 0$  our results indicate a decrease in the signal decay rate. This is supported by expression (48) for the non-confined signal, containing two non-decaying traveling wave components at  $\text{Kn} \rightarrow 0$ , centered about  $x = 1 \pm \sqrt{5/6} t$  and propagating in the positive and negative  $x$ -directions.

Figure 5 examines the effect of wall conditions on the acoustic pressure at continuum-limit conditions. Maintaining  $\text{Kn} = 0.02$  as in Fig. 4, higher pressure amplitudes, compared with their counterparts in the nearly-free-molecular regime (cf. Fig. 2), are observed. Here, the specular- and adiabatic-wall systems exhibit essentially identical waveforms, as discussed in the beginning of Sec. 4.3.2 and mentioned after Eq. (48). The isothermal-wall condition yields the weakest wall reflection, similar to the free-molecular result shown in Fig. 2. Consequently, different from the nearly equal-amplitude double-peak waveform characterizing the specular and adiabatic wall systems (see the black and blue curves in Fig. 5b), the reflected wave in the isothermal-wall setup (marked by the left of the two red peaks in Fig. 5b) decays at a higher rate, and is therefore transmitted to shorter distances from the boundary. Here, again, the heat-absorbing boundary condition appears efficient in confining the wall acoustic reflection to its relative proximity.

Having verified the validity of the NSF model in predicting the system response at  $t/\text{Kn} \gg 1$ , Fig 6 considers the breakdown of the continuum-limit description with decreasing time, and examines the capacity of the R13 model to better capture the gas evolution at shorter times. Taking  $t = 1$ , the figure compares between NSF, R13 and DSMC predictions for an isothermal wall system at  $\text{Kn} = 0.02, 0.05$  and  $0.1$ , corresponding to  $t/\text{Kn} = 50, 20$  and  $10$ . Notably, the R13 scheme predicts the DSMC results better in all cases. This includes the  $\text{Kn} = 0.02$  case (see Fig. 6a), where the near-wall Knudsen-layer behavior and the slight peak about  $x \approx 1$  are better approximated by the dashed blue curve. At  $\text{Kn} = 0.05$  (Fig. 6b), the R13 scheme yields distinctly preferable results over NSF predictions. Increasing  $\text{Kn}$  further to  $\text{Kn} = 0.1$  in Fig. 6c, the breakdown of the R13 description becomes visible, showing discrepancies from DSMC data. Combining with the results in Fig. 3, it is concluded that the free-molecular and near-continuum schemes provide satisfactory descriptions of the system behaviour at times  $t/\text{Kn} \lesssim 2$  and  $t/\text{Kn} \gtrsim 20$ , respectively, whereas the intermediate  $2 \lesssim t/\text{Kn} \lesssim 20$  time interval may be well captured by DSMC calculations only.

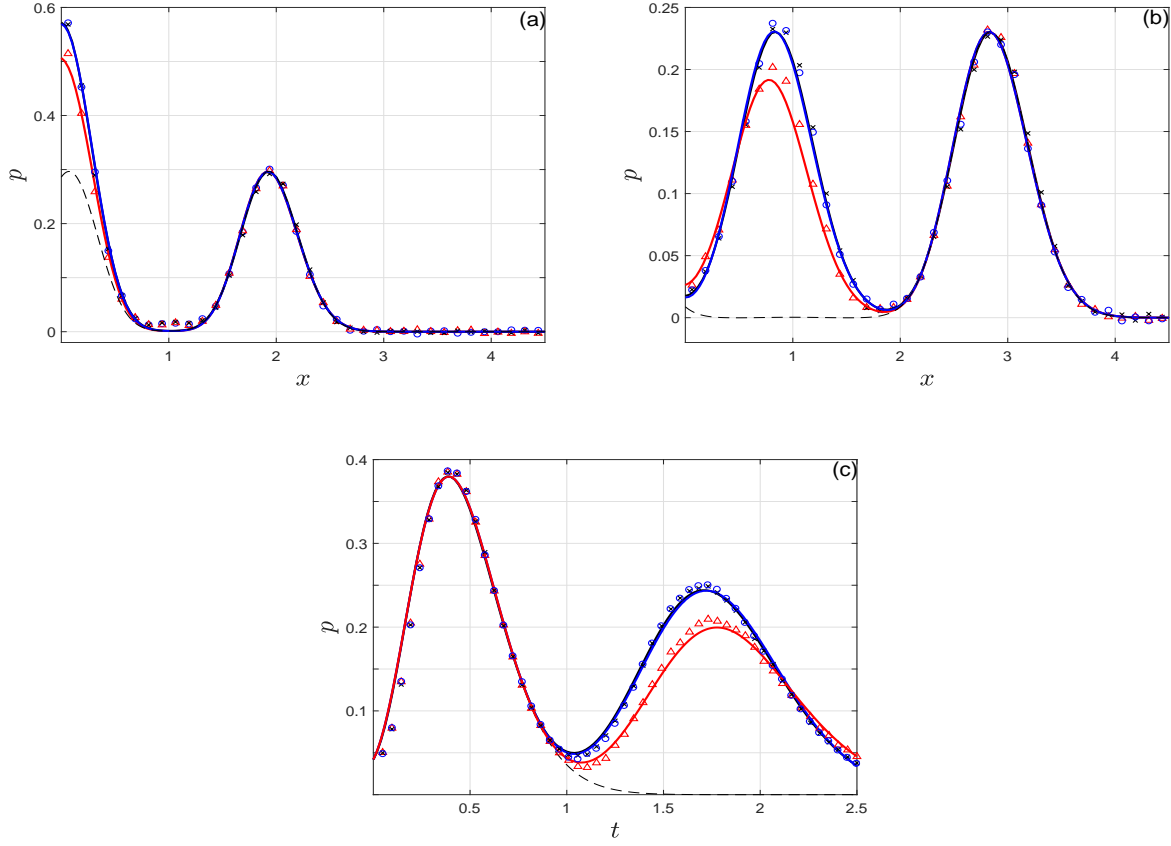


Figure 5: Effect of the wall boundary condition on the acoustic pressure: (a,b) time snapshots at (a)  $t = 1$  and (b)  $t = 2$ ; (c) time variation at a fixed  $x = 0.6$  location. The solid curves and symbols present NSF and DSMC predictions at  $\text{Kn} = 0.02$ , respectively. The black, blue and red notations show results for specular, adiabatic and isothermal wall configurations, respectively. The thin dashed lines depict counterpart results in a non-confined setup.

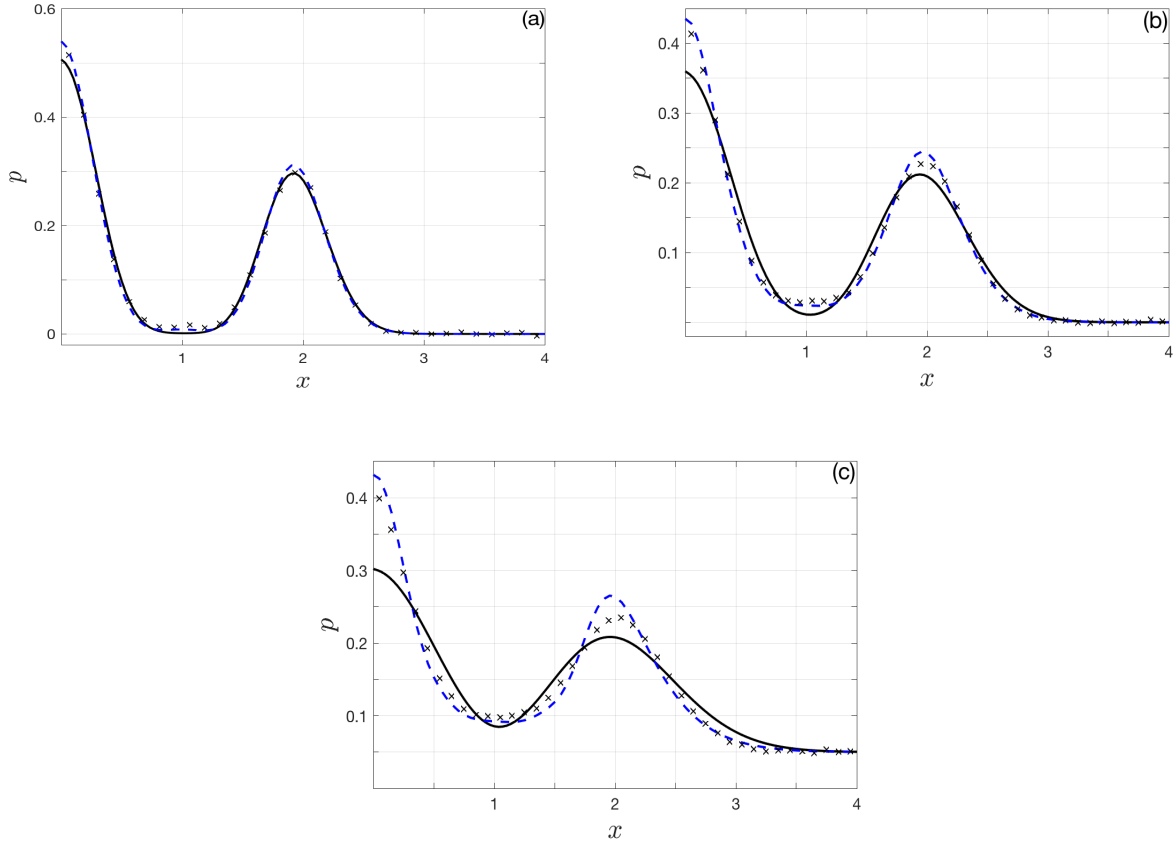


Figure 6: Breakdown of the near-continuum approximations with decreasing  $t/\text{Kn}$ :  $x$ -variations of the acoustic pressure at  $t = 1$  in the NSF (solid lines) and R13 (dashed curves) solutions compared with DSMC results (crosses) at (a)  $\text{Kn} = 0.02$ , (b)  $\text{Kn} = 0.05$  and (c)  $\text{Kn} = 0.1$  for an isothermal wall setup.

### 6.3 The force exerted on the wall

The interaction between the gas and the solid surface results in an unsteady force exerted on the boundary. Applying the linearized  $x$ -momentum balance in the fluid, it is found, regardless of the flow regime, that the  $x$ -directed force acting on the wall is given by

$$F_{\text{wall}}(t) = -\frac{d}{dt} \int_0^\infty u(x, t) dx. \quad (49)$$

In the linearized approximation, the force therefore reflects the rate of change in the gas total momentum. In this section we analyze the effects of gas rarefaction and wall boundary conditions on  $F_{\text{wall}}(t)$ .

Figures 7a and 7b present time-variations of  $F_{\text{wall}}$  at highly-rarefied (Fig. 7a) and near-continuum (Fig. 7b) conditions. The figures compare between specular, adiabatic and isothermal wall systems. In Fig. 7a, free-molecular and  $\text{Kn} = 5$  DSMC results are shown. Fig. 7b presents DSMC and R13-based predictions at  $\text{Kn} = 0.02$ . In common to both figures,  $F_{\text{wall}}(t) < 0$ , indicating a repelling force in the negative  $x$ -direction. The force varies non-monotonically in time, reaching a minimum value [maximum repelling force, denoted hereafter by  $F_{\text{wall}}^{\text{max}} = \max |F_{\text{wall}}(t)|$ ] when the waveform peak reaches the surface. The force amplitude is consistently smallest in the isothermal-wall setup. This is in line with the results in Figs. 2 and 5, indicating that the thermal energy exchange with an isothermal wall yields the transmission of a weaker acoustic disturbance. The specular- and adiabatic-wall forces turn identical in the continuum limit, while  $F_{\text{wall}}^{\text{max}}$  is largest in the specular-wall setup at free-molecular conditions. Inspecting the differences between Figs. 7a and 7b further, it is noted that  $F_{\text{wall}}^{\text{max}}$  is larger in the low- $\text{Kn}$  case for each of the wall setups. Additionally,  $F_{\text{wall}}^{\text{max}}$  occurs at later times in the continuum limit, shifting from  $t_{\text{wall}}^{\text{max}} \approx 0.61$  at  $\text{Kn} \rightarrow \infty$  to  $t_{\text{wall}}^{\text{max}} \approx 1.01$  at  $\text{Kn} = 0.02$ .

To gain further insight into these observations, Fig. 7c presents the variation of  $F_{\text{wall}}^{\text{max}}$  with  $\text{Kn}$  for each of the wall-condition configurations. Free molecular, DSMC and R13-based results are presented. Since  $t_{\text{wall}}^{\text{max}} \sim O(1)$  in all cases, it is expected and confirmed that the free-molecular and R13 approximations hold at  $\text{Kn} \gg 1$  and  $\text{Kn} \ll 1$ , respectively. The intermediate interval of  $0.1 \lesssim \text{Kn} \lesssim 1$  is captured via DSMC calculations. Primarily, the figure indicates an increase

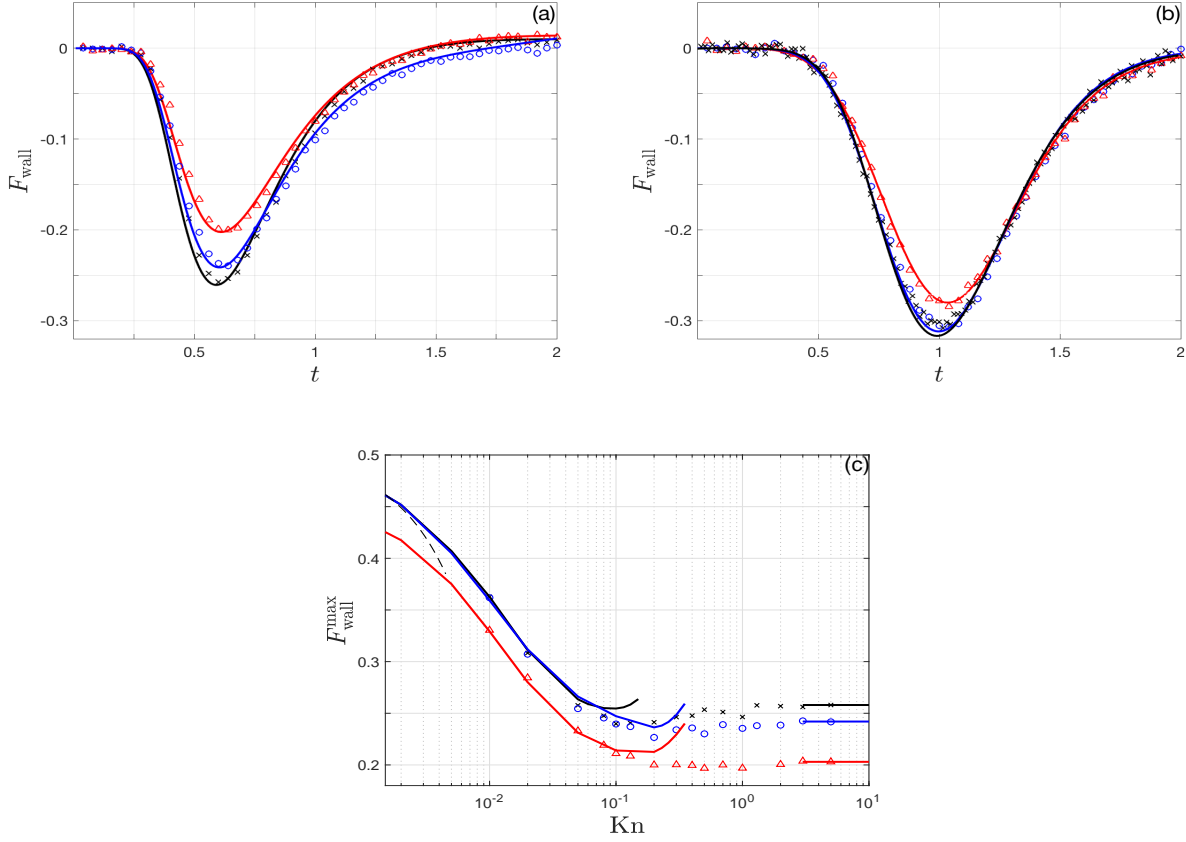


Figure 7: Effects of gas rarefaction and wall boundary conditions on the normal force exerted on the boundary: (a,b) time-variations of  $F_{\text{wall}}$  at (a)  $\text{Kn} = 5$  and (b)  $\text{Kn} = 0.02$ ; (c)  $\text{Kn}$ -variation of the maximum repelling force,  $F_{\text{wall}}^{\text{max}} = \max |F_{\text{wall}}(t)|$ . The black, blue and red notations mark results for specular, adiabatic and isothermal wall setups, respectively. The symbols denote DSMC predictions, whereas the solid curves show free-molecular- (in Fig. 7a and in Fig. 7c at  $\text{Kn} \gg 1$ ) or R13-based (in Fig. 7b and in Fig. 7c at  $\text{Kn} \ll 1$ ) results. The thin dashed line in Fig. 7c marks the asymptote in Eq. (50).

in  $F_{\text{wall}}^{\text{max}}$  with decreasing Kn. This is rationalized by recalling the rapid decay of the initial perturbation in the free-molecular limit compared with the near-continuum regime (cf. the wave amplitudes in Figs. 1 and 4). The interaction between the transmitted perturbation and the surface is then more intense at lower Kn, leading to the general increase in  $F_{\text{wall}}^{\text{max}}$ .

Applying the closed-form approximations obtained in the NSF [see Eq. (48) *et seq.*] and free-molecular (see Appendix B) limits, some quantitative evaluations for  $F_{\text{wall}}^{\text{max}}$  and  $t_{\text{wall}}^{\text{max}}$  may be derived. Starting with the continuum limit, we apply  $T^{(\text{no-wall})}(x, t)$  in Eq. (48) to obtain  $T^{(\text{spec})}(x, t)$  and  $u^{(\text{spec})}(x, t)$ , and approximate the force on a specular wall using Eq. (49). Keeping the leading order in  $\alpha \text{Kn} \ll 1$  and evaluating the force extremal value, we find

$$F_{\text{wall}}^{\text{max}}(\text{Kn} \ll 1) \approx \frac{1}{2} - \frac{7}{\sqrt{30}} \alpha \text{Kn}, \quad (50)$$

occurring at time

$$t_{\text{wall}}^{\text{max}}(\text{Kn} \ll 1) \approx \sqrt{\frac{6}{5}} - \frac{23}{5} \text{Kn}. \quad (51)$$

The result in Eq. (50) supports the observed trend of a decrease in  $F_{\text{wall}}^{\text{max}}$  with increasing Kn. Similarly, Eq. (51) agrees with the shift noted in  $t_{\text{wall}}^{\text{max}}$  to earlier times with increasing Kn. This shift is attributed to the higher wave speed at free-molecular conditions ( $U_{\text{th}}^*$ ) compared with the continuum limit ( $c_0^*$ ), maintaining the ratio  $U_{\text{th}}^*/c_0^* = \sqrt{6/5}$ . Consequently, the disturbance wavefront reaches the boundary at earlier times for larger Kn, resulting in a decrease in  $t_{\text{wall}}^{\text{max}}$ . Note that approximations (50) and (51) hold for setups where  $\alpha \gg 1$ . Combined with the above  $\alpha \text{Kn} \ll 1$  restriction, the applicability of the NSF-based maximum-force evaluation is limited to particularly small Knudsen numbers, as demonstrated by the narrow  $\text{Kn} \ll 1$  interval where the dashed and solid lines in Fig. 7c match.

Focusing on the free-molecular limit, the analyses in Sec. 3 and Appendix B may be applied to approximate the wall force. To this end, it may be readily established that the free-molecular force on an adiabatic wall is given by

$$F_{\text{wall}}^{(\text{ad})}(t; \text{Kn} \gg 1) = \frac{1}{4} [\rho_w^{(\text{ad})}(t) + T_w^{(\text{ad})}(t)] + \frac{1}{t\sqrt{\pi}} \int_0^\infty T_{\text{in}}(s) \left[ \left( \frac{s}{t} \right)^4 - \frac{1}{2} \left( \frac{s}{t} \right)^2 \right] ds, \quad (52)$$

whereas the force on an isothermal wall is obtained by replacing  $\rho_w^{(\text{ad})}$  with  $\rho_w^{(\text{iso})}$  and assigning

$T_w^{(\text{ad})} = 0$  in Eq. (52). For the case of a specular boundary,

$$F_{\text{wall}}^{(\text{spec})}(t; \text{Kn} \gg 1) = \frac{2}{t\sqrt{\pi}} \int_0^\infty T_{\text{in}}(s) \left[ \left( \frac{s}{t} \right)^4 - \frac{1}{2} \left( \frac{s}{t} \right)^2 \right] ds. \quad (53)$$

The time  $t_{\text{wall}}^{\text{max}}(\text{Kn} \gg 1)$  of maximum force may subsequently be approximated by differentiation of the respective expressions for  $F_{\text{wall}}$ . Markedly, for  $\alpha \gg 1$  we find that

$$t_{\text{wall}}^{\text{max}}(\text{Kn} \gg 1) \approx \left[ 2 \left( 1 - \sqrt{2/3} \right) \right]^{1/2} \approx 0.61, \quad (54)$$

regardless of the wall boundary condition and  $\alpha \gg 1$ . This result is supported by the findings in Fig. 7a, indicating that, different from the maximum force amplitude, the time of maximal loading is nearly independent of the wall properties, and is considerably shorter in the free-molecular compared with the near-continuum regime [cf. Eq. (51)].

While the general trend of decreasing  $F_{\text{wall}}^{\text{max}}$  with increasing Kn is dominant, closer inspection of the results Fig. 7c reveals that non-monotonic variations in  $F_{\text{wall}}^{\text{max}}$  occur at intermediate Knudsen numbers. This is particularly visible in the specular-wall setup, yet also obtained in the adiabatic- and isothermal-boundary configurations. Having described the simultaneous mechanisms of wave increasing decay rate and higher expansion speed with increasing Kn, it is the combination of the two that results in the non-monotonic behavior. Specifically, although the perturbation decays faster at larger Kn, it reaches the boundary at an earlier time – which, at intermediate flow conditions, equals or overcomes the weakening rate of the disturbance. Although our limit-case analyses could not capture the intermediate-flow regime accurately, the R13 model was able to describe this phenomenon qualitatively, as depicted by the minima obtained in all left-side curves in Fig. 7c. Further analysis, not followed here, may be carried out using higher order moment schemes or large-Kn asymptotic corrections to the free-molecular description, to better approximate the system behavior at intermediate states. This is encouraged by previous investigations of the (physically different yet topologically similar) Knudsen minimum phenomenon in microchannel flow (recently revisited in Ref. [43]), which was successfully captured via application of generalized hydrodynamic models (e.g., Refs. [44, 45]).

## 7 Conclusion

We investigated the effect of a rigid boundary on the propagation of thermodynamic disturbances in a gas at non-continuum conditions. Considering a semi-infinite setup confined by an infinite planar wall, initial gas disturbances were introduced in the form of density and temperature inhomogeneities. The problem was formulated for arbitrary small-amplitude perturbations, and analyzed in the entire range of gas rarefaction rates. Following the gas evolution in time and space, the results obtained describe the system relaxation to equilibrium, with specific emphasis on the effect of the solid surface. Analytical solutions were derived in the free-molecular and near-continuum regimes and compared with direct simulation Monte Carlo predictions. The impact of the solid wall was highlighted by comparing between the unconfined and confined gas responses with different surface conditions, including fully diffuse (adiabatic or isothermal) and fully specular wall reflections. Focusing on a case of an initial temperature disturbance, the results indicated that the system relaxation time shortens with increasing  $Kn$ . Among the wall conditions considered, the isothermal boundary was found to reflect the weakest acoustic disturbance, as part of the energy carried by the impinging wave is absorbed by the surface. The specular and adiabatic wall systems exhibited identical responses in the continuum limit, while departing with increasing  $Kn$  due to higher-order moment effects. An unsteady normal force exerted by the gas on the surface was detected and analyzed. It was found that the force maximum amplitude decreases with increasing  $Kn$  at near-continuum conditions, yet reaches a minimum value at intermediate-flow states and slightly increases towards the free-molecular limit. This was rationalized in terms of the counteracting mechanisms of a faster decay rate and larger propagation speed occurring with increasing departure from continuum.

Having analyzed the general effect of wall conditions on acoustic reflection in a one-dimensional domain, several extensions may be followed. At first, the viability of optimizing the wall conditions to monitor their boundary reflections may be studied. This is motivated by several recent studies [42, 46, 47], suggesting wall-induced thermoacoustic sound as a means for reducing mechanical vibroacoustic noise. In particular, Ref. [46] has experimentally demonstrated the efficiency of the *thermophone*, a sound transducer device based on the mechanism of *Joule*



*heating* for monitoring boundary heat flux, in cancelling out vibroacoustic sound in the continuum limit. While a similar approach is only suggested here as a topic for future study, it seems possible that prescription of a specific time-varying heating profile at the boundary may be useful in controlling the surface back reflection of the acoustic wave viewed in the results. Extension of the current work to a two-dimensional setup, where the expansion of a local two-dimensional source in the vicinity of a boundary is considered, is also desirable. These constitute topics for future investigations.

## Data availability statement

The data that support the findings of this study are available from the corresponding author upon reasonable request.

## Acknowledgment

The research was supported by the ISRAEL SCIENCE FOUNDATION (grant No. 1084/16) and the Aeronautical Engineering Research Fund. Y.B. acknowledges the support by the Adams Fellowship Program of the Israel Academy of Sciences and Humanities.

## A Expressions for the hydrodynamic perturbations in the free-molecular limit

### A.1 Adiabatic-wall system

Substituting Eq. (10) into Eq. (4) and carrying out appropriate quadratures over the molecular velocity space [29], expressions for the macroscopic fields follow. Subtracting the  $O(1)$  uniform leading orders and scaling the remnants by  $\varepsilon$ , the hydrodynamic perturbations in the case of a fully-diffuse adiabatic wall system are obtained for the density,

$$\begin{aligned} \rho^{(\text{ad})}(x, t) = & \frac{1}{t\sqrt{\pi}} \int_0^\infty \left[ \rho_{\text{in}}(s) + T_{\text{in}}(s) \left( \left( \frac{x-s}{t} \right)^2 - \frac{1}{2} \right) \right] \exp \left[ - \left( \frac{x-s}{t} \right)^2 \right] ds + \\ & \frac{x}{\sqrt{\pi}} \int_0^t \frac{1}{(t-s)^2} \left[ \rho_w^{(\text{ad})}(s) + T_w^{(\text{ad})}(s) \left( \left( \frac{x}{t-s} \right)^2 - \frac{1}{2} \right) \right] \exp \left[ - \left( \frac{x}{t-s} \right)^2 \right] ds, \end{aligned} \quad (\text{A1})$$

normal velocity,

$$u^{(\text{ad})}(x, t) = \frac{1}{t\sqrt{\pi}} \int_0^\infty \frac{x-s}{t} \left[ \rho_{\text{in}}(s) + T_{\text{in}}(s) \left( \left( \frac{x-s}{t} \right)^2 - \frac{1}{2} \right) \right] \exp \left[ - \left( \frac{x-s}{t} \right)^2 \right] ds + \frac{x}{\sqrt{\pi}} \int_0^t \frac{x}{(t-s)^3} \left[ \rho_w^{(\text{ad})}(s) + T_w^{(\text{ad})}(s) \left( \left( \frac{x}{t-s} \right)^2 - \frac{1}{2} \right) \right] \exp \left[ - \left( \frac{x}{t-s} \right)^2 \right] ds \quad (\text{A2})$$

and pressure

$$p^{(\text{ad})}(x, t) = \frac{2}{3t^3\sqrt{\pi}} \int_0^\infty (x-s)^2 \left[ \rho_{\text{in}}(s) + T_{\text{in}}(s) \left( \left( \frac{x-s}{t} \right)^2 - \frac{1}{2} \right) \right] \exp \left[ - \left( \frac{x-s}{t} \right)^2 \right] ds + \frac{2}{3t\sqrt{\pi}} \int_0^\infty \left[ \rho_{\text{in}}(s) + T_{\text{in}}(s) \left( \left( \frac{x-s}{t} \right)^2 + \frac{1}{2} \right) \right] \exp \left[ - \left( \frac{x-s}{t} \right)^2 \right] ds + \frac{2x^3}{3\sqrt{\pi}} \int_0^t \frac{1}{(t-s)^4} \left[ \rho_w^{(\text{ad})}(s) + T_w^{(\text{ad})}(s) \left( \left( \frac{x}{t-s} \right)^2 - \frac{1}{2} \right) \right] \exp \left[ - \left( \frac{x}{t-s} \right)^2 \right] ds + \frac{2x}{3\sqrt{\pi}} \int_0^t \frac{1}{(t-s)^2} \left[ \rho_w^{(\text{ad})}(s) + T_w^{(\text{ad})}(s) \left( \left( \frac{x}{t-s} \right)^2 + \frac{1}{2} \right) \right] \exp \left[ - \left( \frac{x}{t-s} \right)^2 \right] ds \quad (\text{A3})$$

fields. The temperature perturbation is given by the linearized form of the equation of state

$$T^{(\text{ad})}(x, t) = p^{(\text{ad})}(x, t) - \rho^{(\text{ad})}(x, t). \quad (\text{A4})$$

## A.2 Specular-wall system

Substituting Eq. (16) into Eq. (4) and carrying out the velocity-space quadratures similar to Sec.

A.1, the expressions for the density, normal velocity and pressure perturbations are

$$\rho^{(\text{spec})}(x, t) = \frac{1}{t\sqrt{\pi}} \int_0^\infty \left[ \rho_{\text{in}}(s) + T_{\text{in}}(s) \left( \left( \frac{x-s}{t} \right)^2 - \frac{1}{2} \right) \right] \exp \left[ - \left( \frac{x-s}{t} \right)^2 \right] ds + \frac{1}{t\sqrt{\pi}} \int_0^\infty \left[ \rho_{\text{in}}(s) + T_{\text{in}}(s) \left( \left( \frac{x+s}{t} \right)^2 - \frac{1}{2} \right) \right] \exp \left[ - \left( \frac{x+s}{t} \right)^2 \right] ds, \quad (\text{A5})$$

$$u^{(\text{spec})}(x, t) = \frac{1}{t\sqrt{\pi}} \int_0^\infty \frac{x-s}{t} \left[ \rho_{\text{in}}(s) + T_{\text{in}}(s) \left( \left( \frac{x-s}{t} \right)^2 - \frac{1}{2} \right) \right] \exp \left[ - \left( \frac{x-s}{t} \right)^2 \right] ds + \frac{1}{t\sqrt{\pi}} \int_0^\infty \frac{x+s}{t} \left[ \rho_{\text{in}}(s) + T_{\text{in}}(s) \left( \left( \frac{x+s}{t} \right)^2 - \frac{1}{2} \right) \right] \exp \left[ - \left( \frac{x+s}{t} \right)^2 \right] ds \quad (\text{A6})$$

and

$$\begin{aligned}
p^{(\text{spec})}(x, t) = & \frac{2}{3t\sqrt{\pi}} \int_0^\infty \left[ \left( \left( \frac{x-s}{t} \right)^2 + 1 \right) \rho_{\text{in}}(s) + \left( \left( \frac{x-s}{t} \right)^4 + \frac{1}{2} \left( \frac{x-s}{t} \right)^2 + \frac{1}{2} \right) T_{\text{in}}(s) \right] \exp \left[ - \left( \frac{x-s}{t} \right)^2 \right] ds + \\
& \frac{2}{3t\sqrt{\pi}} \int_0^\infty \left[ \left( \left( \frac{x+s}{t} \right)^2 + 1 \right) \rho_{\text{in}}(s) + \left( \left( \frac{x+s}{t} \right)^4 + \frac{1}{2} \left( \frac{x+s}{t} \right)^2 + \frac{1}{2} \right) T_{\text{in}}(s) \right] \exp \left[ - \left( \frac{x+s}{t} \right)^2 \right] ds, \quad (\text{A7})
\end{aligned}$$

respectively. The temperature perturbation is given by the linearized form of the equation of state, as in Eq. (A4).

## B Expressions for the wall functions in the free-molecular limit

Substituting Eq. (47) into Eq. (13) and carrying out the specified integrations, the expressions for the wall functions for an adiabatic-wall system are

$$\begin{aligned}
\rho_w^{(\text{ad})}(t) = & \frac{1}{8(1+\alpha t^2)^5} \left\{ \frac{\sqrt{\pi}\alpha t}{\sqrt{1+\alpha t^2}} \left[ 1 + \text{erf} \left( \frac{\alpha t}{\sqrt{1+\alpha t^2}} \right) \right] \exp \left( - \frac{\alpha}{1+\alpha t^2} \right) \right. \\
& \times \left[ -7\alpha^4 t^8 + \left( 11\alpha^4 - \frac{23}{2}\alpha^3 \right) t^6 + (-2\alpha^4 + 12\alpha^3) t^4 + \left( \alpha^2 + \frac{13}{2}\alpha \right) t^2 + 2 \right] \\
& \left. + \exp(-\alpha) \left[ -7\alpha^4 t^8 + (11\alpha^4 - 17\alpha^3) t^6 + (-2\alpha^4 + 13\alpha^3 - 13\alpha^2) t^4 + (2\alpha^2 - 3\alpha) t^2 \right] \right\} \quad (\text{B1})
\end{aligned}$$

and

$$\begin{aligned}
T_w^{(\text{ad})}(t) = & \frac{1}{4(1+\alpha t^2)^5} \left\{ \frac{\sqrt{\pi}\alpha t}{\sqrt{1+\alpha t^2}} \left[ 1 + \text{erf} \left( \frac{\alpha t}{\sqrt{1+\alpha t^2}} \right) \right] \exp \left( - \frac{\alpha}{1+\alpha t^2} \right) \right. \\
& \times \left[ 3\alpha^4 t^8 + \left( -3\alpha^4 + \frac{15}{2}\alpha^3 \right) t^6 + (2\alpha^4 + 4\alpha^3 + 12\alpha^2) t^4 + \left( 7\alpha^2 + \frac{27}{2}\alpha \right) t^2 + 6 \right] \\
& \left. + \exp(-\alpha) \left[ 3\alpha^4 t^8 + (-3\alpha^4 + 9\alpha^3) t^6 + (2\alpha^4 + 3\alpha^3 + 13\alpha^2) t^4 + (6\alpha^2 + 11\alpha) t^2 + 4 \right] \right\}. \quad (\text{B2})
\end{aligned}$$

Similarly, substituting Eq. (47) into Eq. (14), we obtain for the isothermal-wall setup

$$\rho_w^{(\text{iso})}(t) = \frac{1}{(1 + \alpha t^2)^3} \left\{ \frac{\sqrt{\pi} \alpha t}{\sqrt{1 + \alpha t^2}} \left[ 1 + \operatorname{erf} \left( \frac{\alpha t}{\sqrt{1 + \alpha t^2}} \right) \right] \exp \left( -\frac{\alpha}{1 + \alpha t^2} \right) \right. \\ \left. \times \left[ -\frac{1}{2} \alpha^2 t^4 + \left( \alpha^2 + \frac{1}{2} \alpha \right) t^2 + 1 \right] + \exp(-\alpha) \left[ -\frac{1}{2} \alpha^2 t^4 + \alpha^2 t^2 + \frac{1}{2} \right] \right\}. \quad (\text{B3})$$

## References

- [1] A. D. Pierce, *Acoustics*, Springer, Cham, 2019.
- [2] A. Norris, Acoustic cloaking theory, *Proceedings of the Royal Society A* 464 (2008) 2411–2434.
- [3] M. Greenspan, Propagation of sound in five monatomic gases, *The Journal of the Acoustical Society of America* 28 (1956) 644–648.
- [4] L. Sirovich, J. K. Thurber, Propagation of forced sound waves in rarefied gasdynamics, *Journal of the Acoustical Society of America* 37 (1965) 329–339.
- [5] G. Maidanik, H. L. Fox, M. Heckl, Propagation and reflection of sound in rarefied gases. I. Theoretical, *Physics of Fluids* 8 (1965) 259–265.
- [6] S. K. Loyalka, T. C. Cheng, Sound-wave propagation in a rarefied gas, *Physics of Fluids* 22 (1979) 830.
- [7] S. Stefanov, P. Gospodinov, C. Cercignani, Monte Carlo simulation and Navier-Stokes finite difference calculation of unsteady-state rarefied gas flows, *Physics of Fluids* 10 (1998) 289–300.
- [8] N. G. Hadjiconstantinou, Sound wave propagation in transition-regime micro- and nanochannels, *Physics of Fluids* 14 (2002) 802–809.
- [9] A. Manela, N. G. Hadjiconstantinou, On the motion induced in a gas confined in a small-scale gap due to instantaneous boundary heating, *Journal of Fluid Mechanics* 593 (2007) 453–462.

- [10] F. Sharipov, D. Kalempa, Oscillatory Couette flow at arbitrary oscillation frequency over the whole range of the Knudsen number, *Microfluidics and Nanofluidics* 4 (2008) 363–374.
- [11] D. Kalempa, F. Sharipov, Sound propagation through a rarefied gas confined between source and receptor at arbitrary Knudsen number and sound frequency, *Physics of Fluids* 21 (2009) 103601.
- [12] A. Manela, N. G. Hadjiconstantinou, Gas-flow animation by unsteady heating in a microchannel, *Physics of Fluids* 22 (2010) 062001.
- [13] H. Struchtrup, Resonance in rarefied gases, *Continuum Mechanics and Thermodynamics* 24 (2012) 361–376.
- [14] D. Kalempa, F. Sharipov, Sound propagation through a rarefied gas. influence of the gas-surface interaction, *International Journal of Heat and Fluid Flow* 38 (2012) 190–199.
- [15] T. Tsuji, A. Aoki, Moving boundary problems for a rarefied gas: Spatially one-dimensional case, *Journal of Computational Physics* 250 (2013) 574–600.
- [16] A. Manela, G. A. Radtke, L. Pogorelyuk, On the damping effect of gas rarefaction on propagation of acoustic waves in a microchannel, *Physics of Fluids* 26 (2014) 032001.
- [17] N. G. Hadjiconstantinou, A. L. Garcia, Molecular simulations of sound wave propagation in simple gases, *Physics of Fluids* 13 (2001) 1040–1046.
- [18] N. G. Hadjiconstantinou, O. Simek, Sound propagation at small scales under continuum and non-continuum transport, *Journal of Fluid Mechanics* 488 (2003) 399–408.
- [19] A. D. Handford, P. D. O'Connor, J. B. Anderson, L. N. Long, Predicting absorption and dispersion in acoustics by direct simulation Monte Carlo: Quantum and classical models for molecular relaxation, *Journal of the Acoustical Society of America* 123 (2008) 4118–4126.
- [20] X. Liu, X. Chi, Q. Guo, J. Yang, Study of acoustic wave propagation in micro- and nanochannels, *Wave motion* 76 (2018) 51–60.

- [21] G. Chen, Ballistic-diffusive equations for transient heat conduction from nano to macroscales, *Journal of Heat Transfer* 124 (2002) 320–328.
- [22] D. Y. Tzou, *Macro- to Microscale Heat Transfer*, Wiley, Chichester, UK, 2015.
- [23] D. Y. Tzou, E. J. Pfautsch, Ultrafast heating and thermomechanical coupling induced by femtosecond lasers, *Journal of Heat Transfer* 124 (2002) 320–328.
- [24] J. G. Logan, Propagation of thermal disturbances in rarefied gas flows, *AIAA Journal* 1 (1963) 699–700.
- [25] B. M. Berkovsky, V. G. Bashtovoi, The finite velocity of heat propagation from the viewpoint of the kinetic theory, *International Journal of Heat and Mass Transfer* 20 (1977) 621–626.
- [26] B. Zappoli, D. Bailly, Transport in confined compressible fluid under time-dependent volumetric heat sources, *Physics of Fluids A* 2 (1990) 1771–1779.
- [27] A. Herczynski, D. R. Kassoy, Response of a confined gas to volumetric heating in the absence of gravity. I: Slow transients, *Physics of Fluids A* 3 (1991) 566–577.
- [28] A. L. Danforth, L. N. Long, Nonlinear acoustic simulations using direct simulation Monte Carlo, *Journal of the Acoustical Society of America* 116 (2004) 1948–1955.
- [29] Y. Sone, *Molecular Gas Dynamics: Theory, Techniques, and Applications*, Birkhäuser, Boston, 2007.
- [30] M. N. Kogan, *Rarefied Gas Dynamics*, Plenum, New-York, 1969.
- [31] K. Aoki, C. Baranger, M. Hattori, S. Kosuge, G. Martalo, J. Mathiaud, L. Mieussens, Slip boundary conditions for the compressible Navier-Stokes equations, *Journal of Statistical Physics* 169 (2017) 744–781.
- [32] X. Gu, D. Emerson, A computational strategy for the regularized 13 moment equations with enhanced wall-boundary conditions, *Journal of Computational Physics* 225 (2007) 263–283.

- [33] H. Struchtrup, M. Torrilhon, Regularization of Grad's 13 moment equations: Derivation and linear analysis, *Physics of Fluids* 15 (2003) 2668–2680.
- [34] H. Struchtrup, *Macroscopic Transport Equations for Rarefied Gas Flows*, Springer, Berlin, Heidelberg, 2005.
- [35] M. Torrilhon, Modeling nonequilibrium gas flow based on moment equations, *Annual Review of Fluid Mechanics* 48 (2016) 429–458.
- [36] Y. Ben-Ami, A. Manela, The sound of a pulsating sphere in a rarefied gas: continuum breakdown at short length and time scales, *Journal of Fluid Mechanics* 871 (2019) 668–693.
- [37] G. Bird, *Molecular Gas Dynamics and the Direct Simulation of Gas Flows*, Clarendon, Oxford, 1994.
- [38] Y. Ben Ami, A. Manela, Acoustic field of a pulsating cylinder in a rarefied gas: Thermoviscous and curvature effects, *Physical Review Fluids* 2 (2017) 093401.
- [39] Y. Ben-Ami, A. Manela, Nonlinear thermal effects in unsteady shear flows of a rarefied gas, *Physical Review E* 98 (2018) 033121.
- [40] Y. Ben-Ami, A. Manela, Effect of heat-flux boundary conditions on the Rayleigh-Bénard instability in a rarefied gas, *Physical Review Fluids* 4 (2019) 033402.
- [41] Y. Ben-Ami, A. Manela, Acoustic wave propagation at non-adiabatic conditions: the continuum limit of a thin acoustic layer, *Physical Review Fluids* 5 (2020) 033401.
- [42] A. Manela, L. Pogorelyuk, Active noise control of a vibrating surface: Continuum and non-continuum investigations on vibroacoustic sound reduction by a secondary heat-flux source, *Journal of Sound and Vibration* 358 (2015) 20–34.
- [43] W. Liu, G. Tang, W. Su, L. Wu, Y. Zhang, Rarefaction throttling effect: Influence of the bend in micro-channel gaseous flow, *Physics of Fluids* 30 (2018) 082002.
- [44] H. Struchtrup, M. Torrilhon, Higher-order effects in rarefied channel flows, *Physical Review E* 78 (2008) 046301.

- [45] B. Eu, Normal stress effects on Knudsen flow, *Physics of Fluids* 30 (2018) 013103.
- [46] S. Julius, R. Gold, A. Kleiman, B. Leizeronok, B. Cukurel, Modeling and experimental demonstration of heat flux driven noise cancellation on source boundary, *Journal of Sound and Vibration* 434 (2018) 442–455.
- [47] A. Manela, L. Pogorelyuk, Cloaking via heating: Approach to acoustic cloaking of an actuated boundary in a rarefied gas, *Physics of Fluids* 26 (2014) 062003.